SKI Report 2008:06

Research

Synthetic Aperture Focusing Technique in Ultrasonic Inspection of Coarse Grained Materials

Tadeusz Stepinski

December 2007

ISSN 1104-1374
ISRN SKI-R-08/06-SE

SKI

SKI perspective

This report presents the results of an investigation of SAFT algorithms as applied for post-processing of ultrasonic data acquired for inspection of coarse grained materials. Ultrasonic inspection of coarse grained material is associated with higher noise and lower efficiency than other material. This report is one step towards understanding these effects and to developing suitable methodology to inspect coarse grained materials.

Project information

Responsible for the project at SKI has been Peter Merck.
SKI reference: 14.43 - 200543110

SKI Report 2008:06

Research

Synthetic Aperture Focusing Technique in Ultrasonic Inspection of Coarse Grained Materials

Tadeusz Stepinski

Uppsala Universitet
Signals and Systems
Box 528
SE-751 20 Uppsala
Sweden

December 2007

Abstract

Experience from the ultrasonic inspection of nuclear power plants has shown that large focused transducers are relatively effective in suppressing grain (structure) noise. Operation of a large focused transducer can be thought of as an integration (coherent summation) of individual beams reflected from the target and received by individual points at the transducer surface.

Synthetic aperture focusing technique (SAFT), in its simplest version mimics an acoustic lens used for focusing beams at a desired point in the region of interest. Thus, SAFT should be able to suppress the grain noise in the similar way as the focused transducer does.

This report presents the results of investigation of SAFT algorithms applied for post-processing of ultrasonic data acquired in inspection of coarse grained metals. The performance of SAFT in terms of its spatial (cross-range) resolution and grain noise suppression is studied. The evaluation is made based on the experimental data obtained from the ultrasonic inspection of test specimens with artificial defects (side drilled holes). SAFT algorithms for both contact and immersion mode are introduced and experimentally verified.

Contents

List of Figures

Chapter 1

Introduction

Ultrasonic images show a characteristic granular structure commonly known as speckle in medical applications and grain (structure) noise in NDE. Speckle in ultrasonic images arises from the presence of tiny scatterers in the range cell. The scattering from these tiny targets gives rise to an addition of the phasors, resulting in fluctuations in the amplitude of the echo. Thus the presence of the scatterers along with the inherent coherence of the (sound) sources gives rise to these amplitude fluctuations called speckle. The speckle, which is a common artifact of diffraction limited imaging, reduces the detection capability of ultrasonic imaging systems and indirectly affects the identification of specific reflectors in the regions of interest (ROI).

Speckle can be reduced through diversity techniques resulting in increased contrast of the image. The diversity techniques involve averaging the multiple images created either through frequency compounding or spatial compounding. Frequency compounding involves decomposition of an image obtained with a broadband transducer into a number of narrowband images and detecting correlations between those images. Split spectrum processing (SSP) is well known technique belonging to this class.

In spatial compounding, the multiple images are produced by viewing the ROI from various spatial locations, angles or orientations of a transducer. Spatial compounding reduces speckle and increases image contrast by incoherently averaging different images of the same ROI. The term incoherent means that the envelope of the RF A-scans is calculated first, and then a brightness B-scan is obtained by aggregating those A-scans (this is a standard way of presenting results in medical applications). The compound images are generated by performing different types of averaging of the obtained B-scan images, for example, mean, median, root-mean-square or geometric mean.

Coherent averaging of RF images is generally difficult in medical applications due to tissue movements and inaccurately known transducer position. However, the situation in most NDE applications is different since the test object is stationary and transducer position can be measured very accurately.

Experience from the inspection of nuclear reactors has shown that large focused transducers are relatively effective in suppressing grain noise. Operation of a large focused transducer can be thought of as integration (coherent summation) of the individual beams reflected from the target and received by individual points at the transducer surface. The use of such transducers, however, is limited by practical reasons – they are bulky and inflexible (fixed focus).

Recently, advanced synthetic aperture (SA) algorithms characterized by an enhanced spatial resolution, especially in near fieldhave developed in our group. SA algorithms are based on

coherent summation of ultrasonic signals received by a transducer in different locations. SA algorithms are inspired by the synthetic aperture techniques developed and successfully applied in radar (synthetic aperture radar) and sonar (synthetic aperture sonar). In the simplest version, the SA algorithm mimics a physical lens focusing beams in a desired point of ROI. The advantage, however, is that by a suitable post-processing of the received A-scans SA can produce the focusing effect in all points of ROI simultaneously.

The main aim of this preliminary study is to investigate performance of SA used for the inspection of grainy materials in terms of grain noise suppression. We apply advanced SA algorithms to signals (B-scans) acquired from the test blocks characterized by large grains. The blocks have a number of representative artificial defects that are difficult to detect using standard means. The inspection is performed in contact and in immersion using standard transducers.

The first step of this project has been performed in the form of two diploma works [1, 2] that are summarized in the following chapters.

Chapter 2

SAFT in the Time Domain

In SAFT the pulse-echo measurements made at a multitude of transmitter/receiver locations are combined to form a map of the ultrasonic reflectivity of the insonified region of interest (ROI). The method takes advantage of both spatial and temporal correlations to enhance the resolution and the signal-to-noise ratio of the resultant images. Time-domain SAFT (t-d SAFT) has been used in ultrasonic NDE mainly due to its two benefits: first, it is capable of improving lateral resolution in the focal zone, and second, it extends the focal zone resulting in a dynamic focusing effect [3, 4].

It is worth noting, however, that the performance of SAFT in practical applications, depends on the particular implementation of the SAFT algorithm as well as on the size of the transducer used in synthetic aperture [5]. Usually, the NDE SAFT implementations are performed using a delay-and-sum (DAS) processing in time-domain [4, 6]. DAS is a straightforward way of simulating the desired lens effect, commonly used in phased arrays. Majority of SAFT implementations is based on a very simplified model of the imaging system that has been used in radar and sonar applications. When those algorithms are applied in NDE diffraction effects of the transducer, related to its size may impair image quality.

In our opinion it is important to investigate advantages and disadvantages of SAFT in various NDE applications to identify those problems that are related to particular SAFT implementations. It is also of importance to investigate SAFT performance in inspection of coarse grained materials used in nuclear power plants.

In this chapter, the time domain SAFT algorithm based on the DAS principle is particularly studied. The discussion is confined to the monostatic case where a single unfocused finite-aperture transducer is moves along the horizontal axis.

Usually, there is no prior knowledge about the defect positions in material, and the dynamic focusing in the region of interest (ROI) is performed to achieve the improved cross-range resolution. Different delays are applied in the DAS algorithm to simulate the specific hyperbolas that simply express the distances from the elements in the aperture to the focus point.

2.1 t-d SAFT Algorithm in the contact mode

Let us illustrate the SAFT principle with a simple system model. Consider the measurement setup shown in Figure 2.1, which is known in radar applications as a broadside strip-map mode synthetic aperture imaging system. This means that the SAFT system maintains its transducer

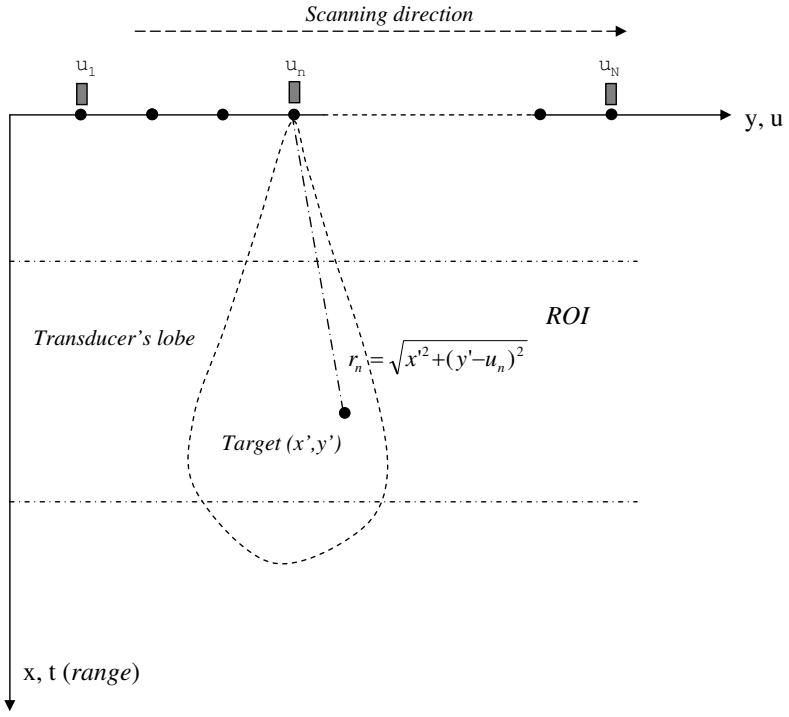

Figure 2.1: 2D geometry appropriate for broadside strip-map mode synthetic aperture.

beam at a broadside thoughout the data acquisition period.

The region of interest (ROI) contains a number of reflecting targets (flaws) in the spatial (x, y) domain, where x is called the range while y identifies the cross range. The transducer element moves along the u axis, which is parallel to the y axis of the target area, and transmits a broadband pulse.

Assuming that the transducer's radiation pattern is omni-directional, the measured reflected signal at the transducer position u_n is given by [7]

$$e(t, u_n) \approx \int_x \int_y f(x, y) \cdot b(t, x, y - u_n) *_t p\left(t - \frac{2}{c}\sqrt{x^2 + (y - u_n)^2}\right) dxdy \tag{2.1}$$

where $b(t, x, y)$ is the spatial-temporal response of the combined transmitter and receiver apertures and the symbol $*_t$ represents convolution in the time domain.

To achieve focus at an observation point (x', y') in the ROI, the SAFT time-shifts and performs a summation of the received signals $e(t, u_n)$ measured at transducer positions u_n for all n in the synthetic aperture. Assuming that the point source element model is valid (that is the ROI is in the transducer's far-field), the DAS scheme of a t-d SAFT is illustrated by the block diagram shown in Figure 2.2. The time delays, denoted by τ_n, aiming to compensate for different pulse traveling time, can be expressed as

$$\tau_n = \frac{2}{c}(r_n - x') = \frac{2}{c}(\sqrt{x'^2 + (y' - u_n)^2} - x') \tag{2.2}$$

for $n = 1, 2, ..., N$, where N is the number of element positions, r_n is the distance from the element at position u_n to the observation point. A smooth apodization a_n, known as windowing

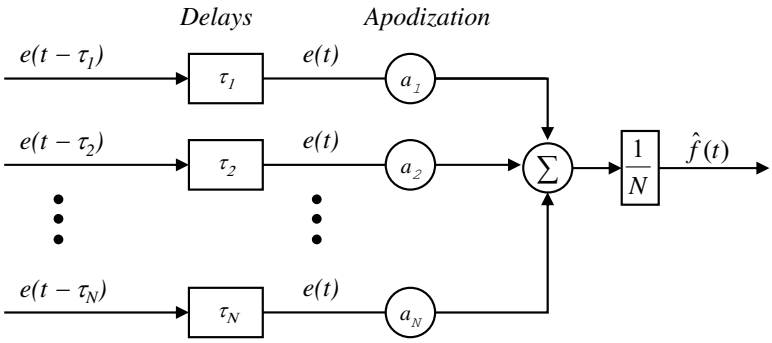

Figure 2.2: Block diagram for the delay-and-sum SAFT system. DAS generates a sum of delayed signals received at different transducer positions. Each signal can also be multiplied by the apodization coefficient to reduce the side lobes in the resulting beampattern.

in spectral analysis, is a simple method to control the side lobe levels. After time shifts and summation, the final image is

$$i(x', y') = \sum_{n=0}^{L-1} \frac{a_n e(t - \frac{x'}{c}, u_n)\delta(t - \tau_n)}{r_n} \tag{2.3}$$

where the factor $r_n = \sqrt{x'^2 + (y' - u_n)^2}$ is due to the propagation attenuation.

For the conventional DAS, used in array fixed focus phased arrays, a certain range R, which is the distance from the middle of the ROI to the transducer scanning direction, needs to be specified to determine the delay vector $[\tau_1, \tau_2, ..., \tau_N]$.

$$\begin{aligned} \tau_1 &= \frac{2}{c}(\sqrt{R^2 + (u_1 - y')^2} - R) \\ \tau_2 &= \frac{2}{c}(\sqrt{R^2 + (u_2 - y')^2} - R) \\ &\vdots \\ \tau_N &= \frac{2}{c}(\sqrt{R^2 + (u_N - y')^2} - R) \end{aligned} \tag{2.4}$$

where y' is the y-coordinate of a target, see Figure 2.1. SAFT, however, provides the *all-depth dynamic focusing* effect that enables achieving uniform cross-range resolution in the ROI. In this case, the delay vectors applied to the ultrasonic signals received at different transducer positions need to be updated for each range in the ROI as follows

$$\begin{aligned} \tau_{1i} &= \frac{2}{c}(\sqrt{x'^2 + (u_1 - y')^2} - x'_i) \\ \tau_{2i} &= \frac{2}{c}(\sqrt{x'^2 + (u_2 - y')^2} - x'_i) \\ &\vdots \\ \tau_{Ni} &= \frac{2}{c}(\sqrt{x'^2 + (u_N - y')^2} - x'_i) \end{aligned} \tag{2.5}$$

where y' and x'_i are the coordinates of targets, see Figure 2.1. Note, that focusing is performed for all target depths x'_i in ROI, which results in all-depth focusing.

This is mainly due to the fact that point scatters with different depths in the media would result in different hyperbola responses. As shown in Figure 2.3, if the transducer at the position A receives an echo from the target O it would be interpreted as the scatter at O' located at the depth $AO' = AO$. After scanning the transducer along the y axis, the hyperbola shown in Figure 2.3 corresponding to the scatter located at point O would appear in the resulting B-scan image. The closer to the synthetic aperture, the sharper the hyperbola would be as shown in the right panel of Figure 2.3.

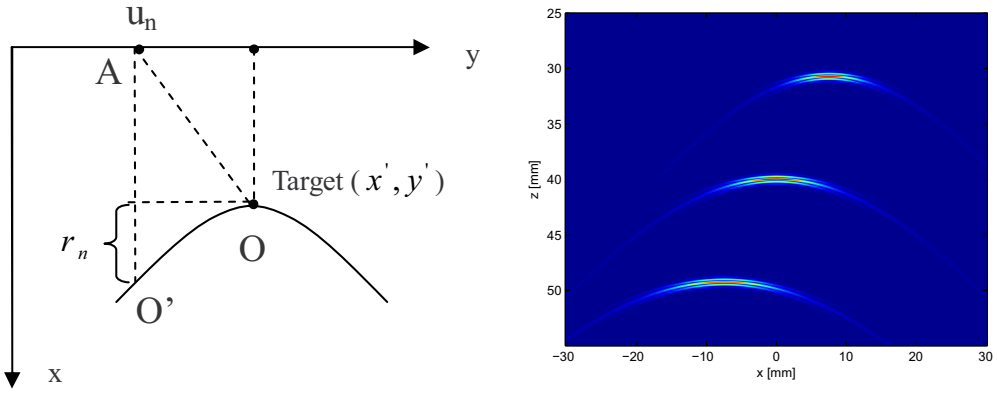

Figure 2.3: Origin of hyperbolic responses in the B-scan data. Forming hyperbolas when transducer is shifted along y axis (left) and the hyperbolas corresponding to the targets located at different range (right).

In SAFT the time shifts specific for each range in the ROI are applied to "shrink" the hyperbolas and obtain the improved cross-range resolution.

2.2 t-d SAFT Algorithm in the immersion mode

Immersion mode, which is a common scanning method in ultrasonic NDE, involves the use of an immersion tank. The object and the transducer are placed under water so that consistent coupling is maintained by the water path as the transducer is moved within the tank.

For the immersion case, the acoustic path between the transducer and the target is no longer a straight line. The difference between water impedance and impedance of the inspected material, for instance, steel results in the beam refraction at the object surface. According to the Fermat principle (expressed in the form of Snell law), the ultrasonic waves of a given length travel along the path between two points which takes the least time.

The real path from the transducer position A to the target scatter O is indicated Figure 2.4 by the solid line with arrows.

Let us denote the beam distance between the probe position u_n and the incident point by s_{wn} and the beam distance between the incidence point and the target in the object at (x', y')

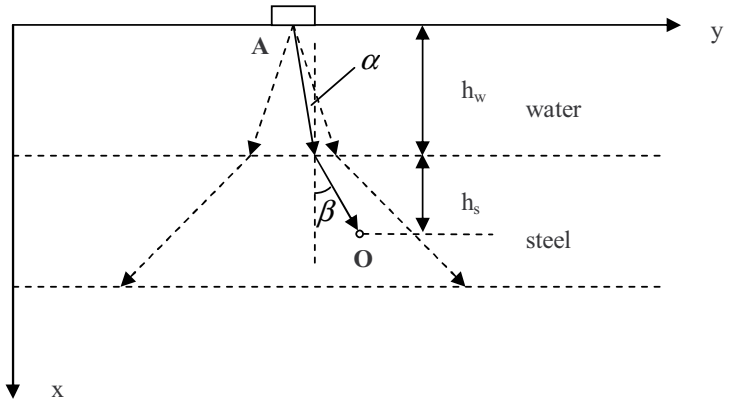

Figure 2.4: Illustration of the Fermat's principle: the ultrasonic wave chooses the path between two points which takes the least time.

by s_{on}. Then the delay vector for the successive transducer positions is

$$\begin{aligned} \tau_1 &= 2[\frac{s_{w1}}{c_w} + \frac{s_{o1}}{c_s}] \\ \tau_2 &= 2[\frac{s_{w2}}{c_w} + \frac{s_{o2}}{c_s}] \\ &\vdots \\ \tau_N &= 2[\frac{s_{wN}}{c_w} + \frac{s_{oN}}{c_s}] \end{aligned} \tag{2.6}$$

where c_w and c_s are acoustic speed in water and steel, respectively. To calculate the delays τ_n the values of s_{wn} and s_{on} have to be found first for each particular setup based on a nonlinear equation resulting from the Fermat principle.

2.3 Effective Aperture Length

In order to determine the number of A-scans that should be included in the synthetic aperture we will introduce the concept of *effective aperture length*. The effective aperture length L_{eff} is motivated by the diffraction effects of the finite-sized transducer. Generally, all transducers have some form of beampattern that takes the form of a main lobe accompanied by a number of side lobes. The main lobe width is an important parameter that defines the transducer's cross-range resolution.

The parameter L_{eff} is defined as the largest aperture length corresponding to wavelength λ that contributes to the SAFT performance in terms of its lateral resolution. It is assumed that the signals received by all elements of a synthetic aperture are used efficiently if the L_{eff} is no longer than the half-power lobewidth of the transducer used in the aperture. For a circular transducer with diameter d the half-power lobewidth at a distance R is [8, 9]

$$L_{eff} \cong \frac{R\lambda}{d} \tag{2.7}$$

Thus for a certain transducer (for fixed d and λ), the longer the range, the longer is the L_{eff}. On the other hand, for a fixed range, smaller transducer diameter or lower transducer center frequency also results in longer L_{eff}.

Thus in the algorithms presented above, the L_{eff} depends on the target range and it should be recalculated for each target range.

2.4 SAFT performance

A rough criterion to measure the cross-range resolution of a transducer is defined through the half-power lobewidth (the width between the $-3dB$ points in the main lobe). The half-power lobe width is

$$L_{\text{eff}} \cong \frac{r_0 \lambda}{d} \tag{2.8}$$

where d is the transducer diameter.

An important difference between the focusing the physical phased arrays and the SAFT is that the synthetic aperture have the cross-range resolution finer by a factor of 2 for the same number of elements that transmit and receives signals. Consequently, the SAFT cross range resolution is [8]

$$\delta_{y3dB} \cong \frac{\lambda r_0}{2L_{\text{eff}}} \tag{2.9}$$

where L_{eff} is the effective synthetic aperture length, defined as the largest aperture length corresponding to the ultrasonic frequency that contributes to the SAFT performance in terms of its lateral resolution, and r_0 is the focusing range. Note that Eq.(2.9) illustrates the fact that the synthetic aperture simulates a large physical aperture transducer using only one small element.

It is assumed that the signal received by all elements of a synthetic aperture are used efficiently if the L_{eff} is no longer than the half-power lobewidth of the transducer used in the aperture, given by (2.9). Finally, combination of Eqs.(2.9) and (2.8) gives SAFT cross-range resolution

$$\delta_{y3dB} \cong \frac{d}{2} \tag{2.10}$$

Thus Eq.(2.10) indicates that the cross-range resolution of the SAFT system is independent of the ultrasonic frequency and range if the effective aperture defined by Eq.(2.8) is used for the shortest wavelength in the ultrasonic signal. The smaller the single transducer is used, the finer resolution can be gained. It should be noted, however, that the minimal transducer size is limited by the signal to noise ratio required for target detection.

Another characteristic feature of both SAFT and phased arrays are so-called *grating lobes* that appear in the beampattern due to the discrete nature of those apertures. If strong scatters are present at the azimuth where the grating lobe appears, they would result in ghost responses in the reconstruction image. According to the Nyquist sampling principle, the spatial sampling step along the y-axis in SAFT must fulfill [10]

$$\Delta_u \leq \frac{d}{4} \tag{2.11}$$

2.5 Experimental Illustration

As an illustration of the t-d SAFT algorithm described in former sections we present results of a simple experiment. The experiment was carried out in a water tank were three steel wires of diameter 0.2 mm were immersed at different depths. This scenario can simulate the case

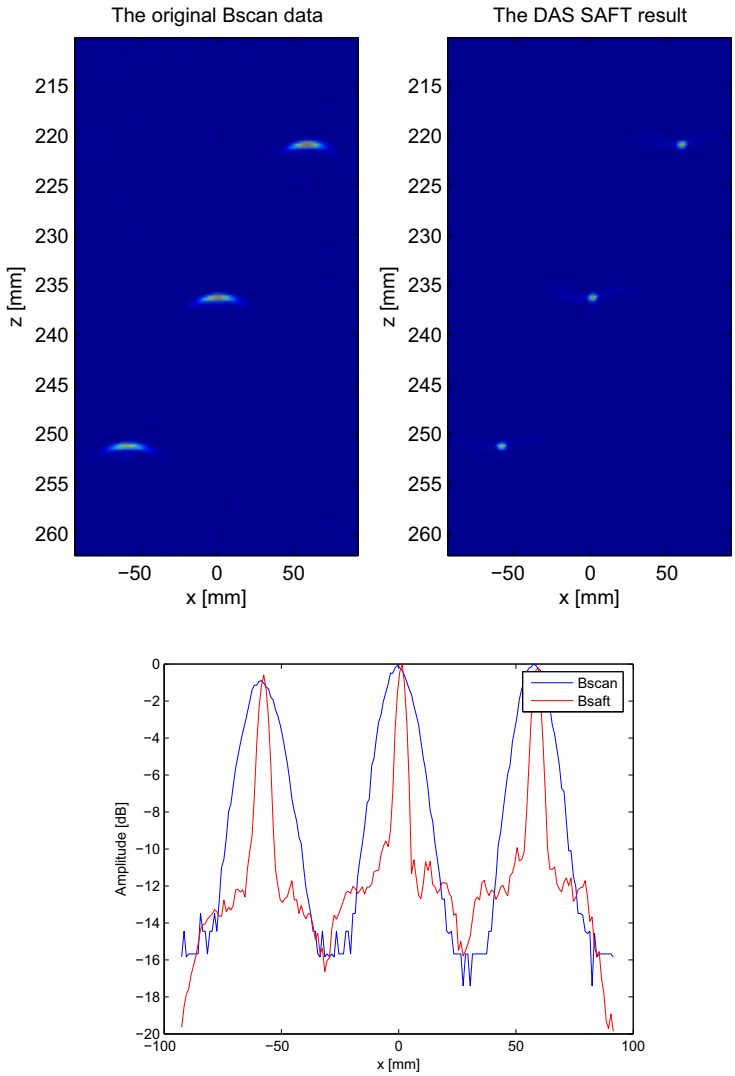

Figure 2.5: Three wires experiment. Raw B-scan (upper left), B-scan after SAFT processing (upper right), and profile plots in dB of both B-scans for the cross-range comparison.

Transducer frequency	2.25 Mhz
Transducer diameter	10 mm
Sound velocity in water	1480 m/s
Sampling frequency	80 MHz
Spatial sampling freq.	1 mm
Synthetic aperture length	40 mm
Bscan 3dB resolution	12.4 mm
Bsaft 3dB resolution	2.9 mm

Table 2.1: Parameters and results of three wires experiment.

where a homogeneous media contains three isotropic flaws at different depths. The experiment parameters are listed in Table 2.1.

The t-d SAFT obviously generates much better result than the original B-scan. According to Table 2.1 and Figure 2.5, the SAFT processing has improved the cross-range resolution in the B-scan more that 4 times.

Also note in Figure 2.6, that the calculated time delay vector fits well to one of the hyperbolas at the raw B-scan.

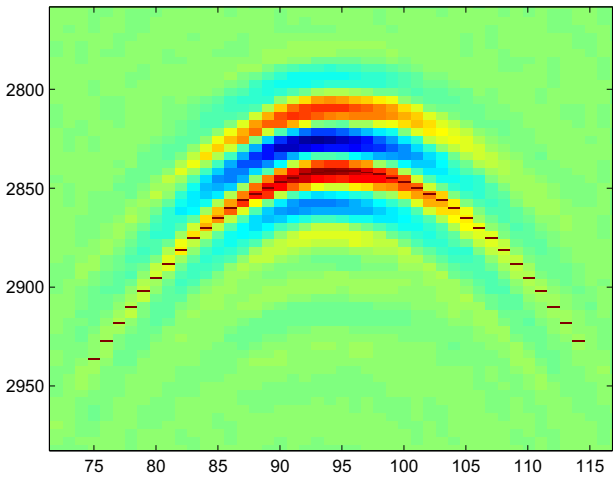

Figure 2.6: Hyperbola fitness comparison in the 3 wires experiment.

This experiment clearly illustrates that the t-d SAFT uses a simple theoretical model for the B-scan response of a point scatter in a homogeneous medium, which turns out to be a hyperbola. However, the responses of realistic transducers characterized by a limited bandwidth do not take the form of very thin hyperbolas but they form a number of parallel hyperbolas in the B-scan (see Figure 2.6).

Chapter 3

Experiments

3.1 Contact Mode Experiments

To verify and test the algorithms discussed in previous chapters, several experiments are performed with various materials and various setups.

3.1.1 Copper Block Experiments

In this experiment a copper block with a number of SDH was inspected in contact mode, for details see [1, 2]. Four side-drilled holes located at the range from 43 mm through 55 mm were imaged. The Panametrics transducer had the center frequency of 2.25MHz and diameter of 0.5". Based on the raw B-scan data, the effective length of synthetic aperture was chosen to 36 mm. The detailed parameters are given at Table 3.1 below. In Figure 3.1 SAFT result can be compared with raw B-scan data. It can be seen that the t-d SAFT yields a substantial resolution improvement. The *-3dB* resolution of SAFT is 4 mm, which is better than the theoretically estimated value, $d/2$=6.35 mm.

3.1.2 Steel Cube Experiments

The test cube #90646 from Ringhals made of cast austenitic steel was inspected in contact mode, for details see [1, 2]. There are two groups of holes that were possible to detect.

Transducer Transducer diameter.	Panametrics 2.25 MHz 12.7 mm
Material velocity	4660 m/s
Sampling freq. Spatial sampling freq.	80 MHz 0.5 mm
Synthetic aperture length	36 mm
B-scan -3dB width SAFT -3dB width d/2	6.25 mm 4.0 mm 6.35 mm

Table 3.1: Parameters of contact copper block experiment.

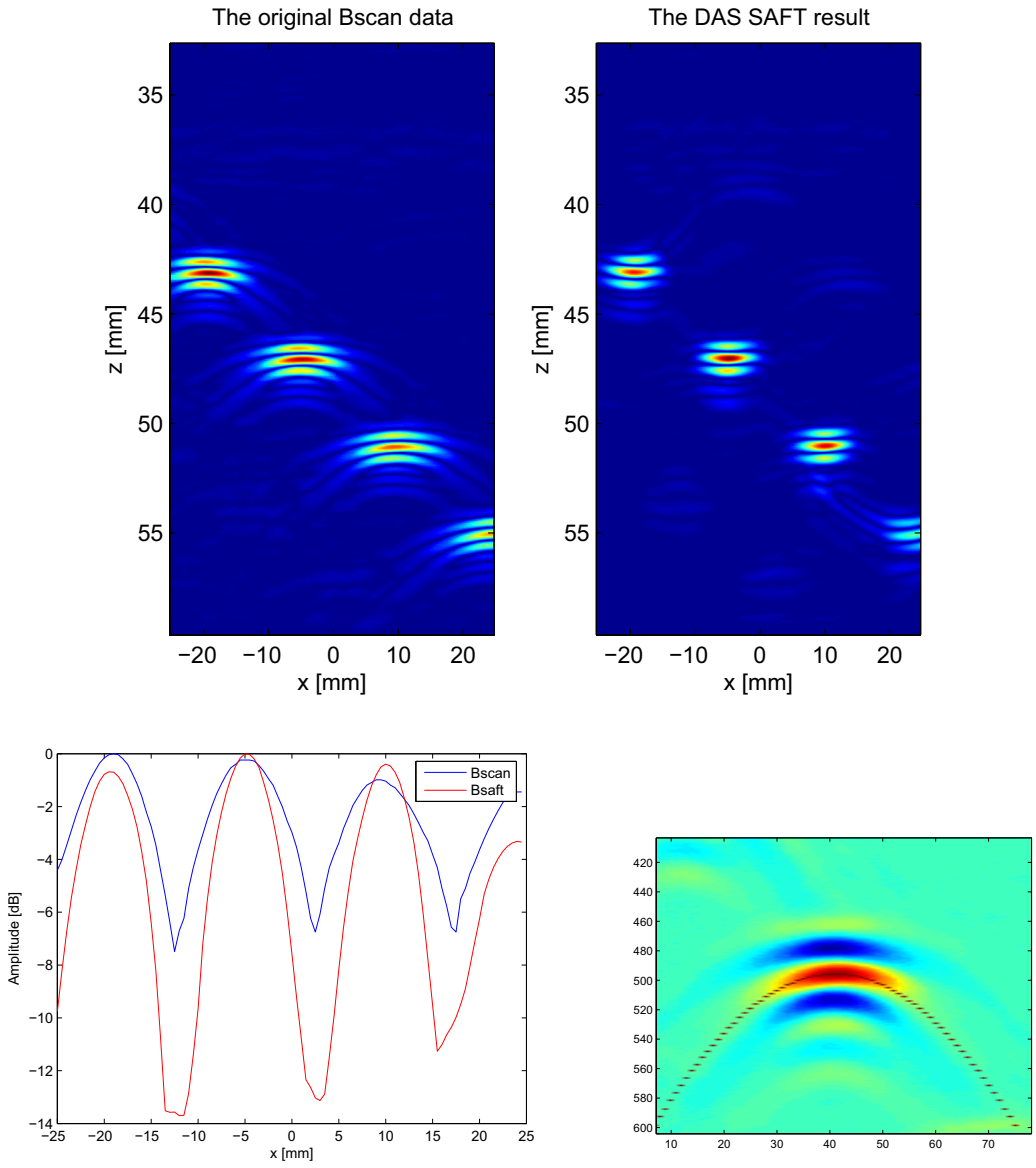

Figure 3.1: B-scan and SAFT result for the copper block experiment (upper). Profiles for the cross-range resolution evaluation of the B-scan and SAFT processed result (lower-left). B-scan and SAFT -3dB widths are respectively $6.25mm$ and $4.0mm$. The simulated hyperbolic time-shift fits well to the shape of the response in B-scan (lower-right).

Transducer Transducer diameter.	Panametrics 2.25 MHz 12.7 mm
Material velocity	5800 m/s
Sampling freq. Spatial sampling freq.	80 MHz 0.5 mm
Synthetic Aperture length	36 mm
B-scan -3dB width SAFT -3dB width d/2	27.3 mm 5.1 mm 6.35 mm

Table 3.2: Test parameters for the steel cube in the first test setup

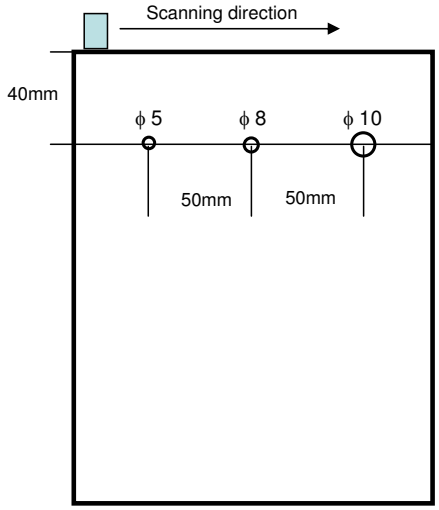

Figure 3.2: The location of the three side-drilled holes in the steel cube in the first test setup.

The **first group of holes** are three side drilled holes (SDHs) with different diameters at the depth of approximately 50 mm. The location of the holes are clearly illustrated in Figure 3.2. The test parameters are listed in Table 3.2.

The original B-scan data and the SAFT results are plotted in Figure 3.3. It can be seen that the resolution of the raw B-scan is quite poor (27.3 mm) and a high level of structure noise is observed. After SAFT processing, the resolution is improved to approx. 5 mm and the noise level has been reduced. The resolution of SAFT is approximately half of the transducer diameter, as discussed previously.

The size of the holes can be estimated from the time of flight at the B-scan responses and the SAFT results. Note, that since the reflections occur at the top of the holes, there are slight differences of the ranges of the three holes in the SAFT processed result. The response to the largest hole (the right one) appears at the shorter range than that of the smallest one.

From lower part of Figure 3.4 it can be seen that the structure noise level after SAFT processing has been decreased with approx. 4 dB comparing with that in the raw B-scan data.

The **second group of holes** that were tested consists of two SDHs that form an angle 45° with the side plane of the cube, see Figure 3.5 (left panel). The transducer was placed in contact

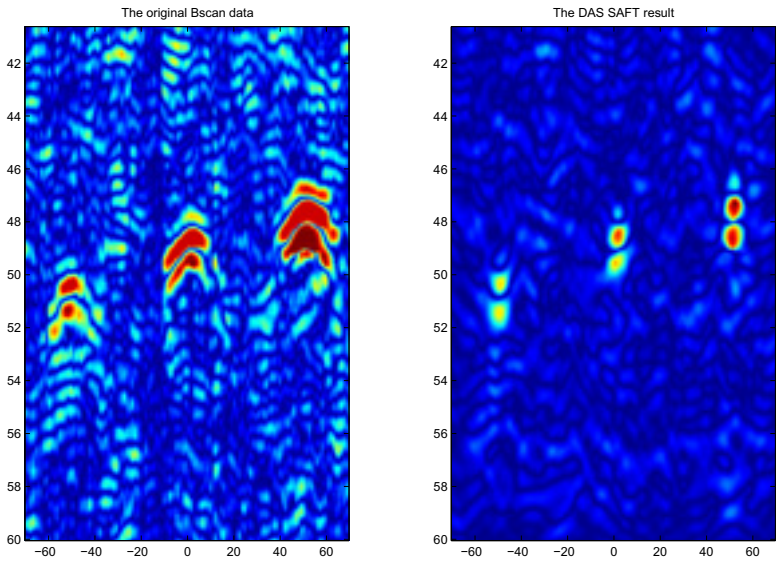

Figure 3.3: Comparison of Bscan and SAFT result of the steel cube in contact mode. The B-scan and SAFT $-3dB$ widths are, respectively 27.3 mm and 5.1 mm.

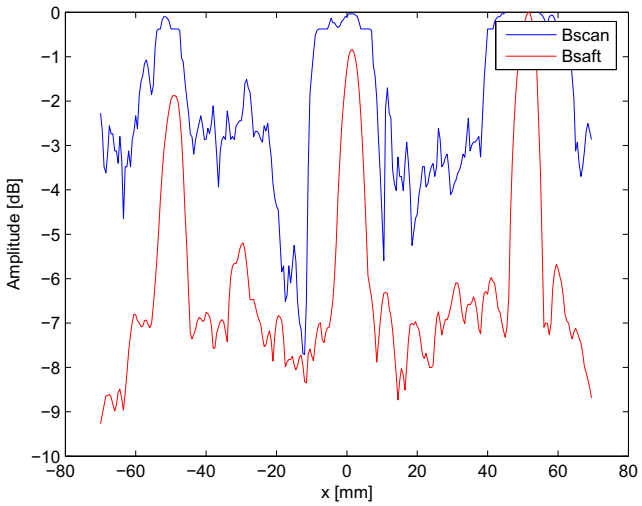

Figure 3.4: Cross-range resolution profiles for steel cube.

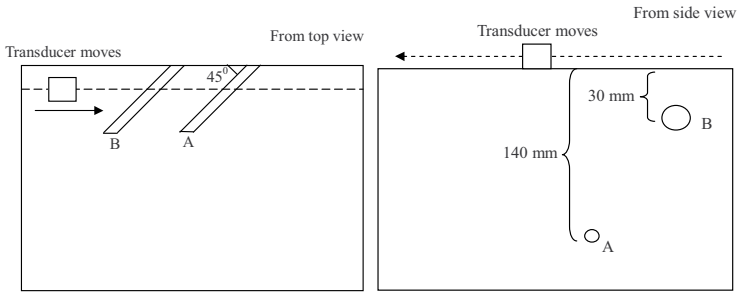

Figure 3.5: Top view (left) and side view (right) of the steel cube in the second test setup.

Transducer freq.	0.5 MHz
Transducer diameter.	35 mm
Material velocity	5800 m/s
Sampling freq.	80 MHz
Spatial sampling freq.	0.5 mm
Synthetic aperture length	36 mm
B-scan -3dB width	68.6 mm
SAFT -3dB width	22.6 mm

Table 3.3: Test parameters for the steel cube in the second test setup

on the top of the cube as shown in Figure 3.5 (right panel).

Due to the long distance in the material to detect holes (especially the hole A in Figure 3.5) the Panametrics transducer with frequency 0.5 MHz was chosen for the test. The transducer diameter was 35 mm. The system parameters are given in table 3.3.

In Figure 3.6, where the test results are presented a considerable structure noise level can be seen. The noise level decreases with depth as the ultrasound is attenuated by the material structure (the distance amplification control was not used). Reflection from the SDH A is clearly pronounced both in the B-scan and the SAFT image but the resolution is approx. 3 times better after the SAFT processing. Reflection from the hole A can be seen at $x = -50mm$ and $y = 135mm$. Although the profiles for both holes are not presented from Figures 3.6 and 3.7 can be seen that the noise level has been improved after the SAFT processing.

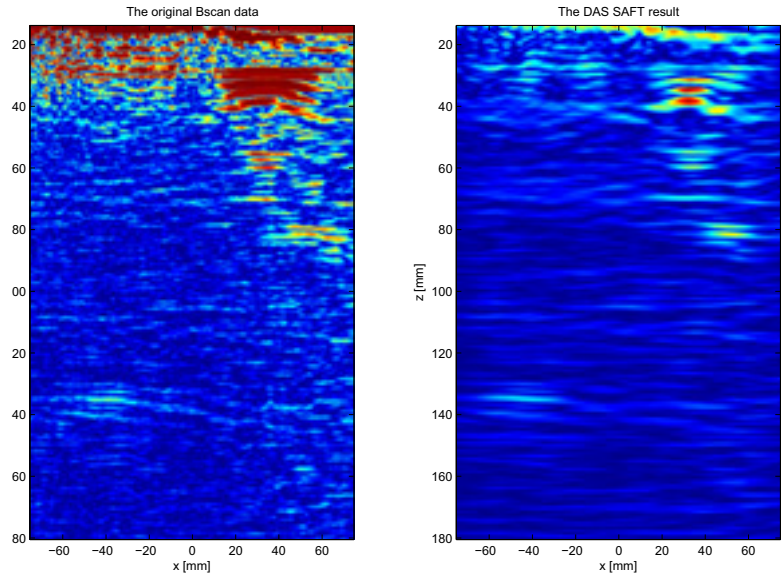

Figure 3.6: B-scan and SAFT results for the steel cube in the second test setup.

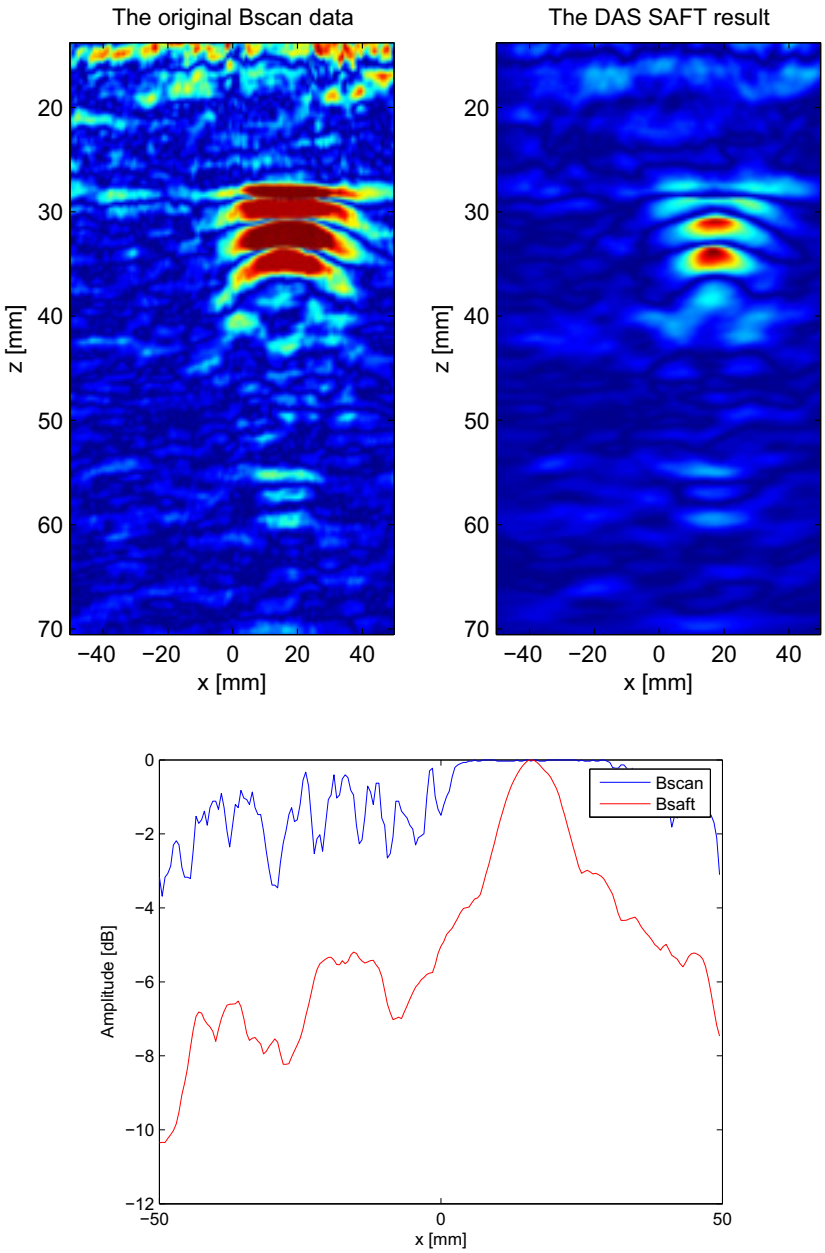

Figure 3.7: Detail of the B-scan and its SAFT result presenting the response of the hole B for the steel cube in the second test setup (upper part). Profiles for the cross-range resolution comparison (lower part). The B-scan -3dB width is 58 mm while SAFT yields the improved resolution of 11.7 mm.

3.2 Immersion Mode Experiments

To verify the immersion version of SAFT algorithm presented in Section immersion tests were performed on two copper test blocks available at our lab, for details see [1].

3.2.1 Copper Block Immersion Mode Experiments

Copper Block I

The copper block with fine structure used in contact experiment reported in Section 3.1.1 was inspected in immersion. This block, referred to as *copper block I* in the sequel, has and a number of SDHs. Three of them located at the depths 23 mm, 27 mm, 31 mm, respectively, from the upper surface were imaged in this test using the Panametrics immersion transducer with diameter 10 mm and frequency 5 MHz. The test parameters are listed in Table 3.4.

Test results are shown in Figure 3.8 where the the B-scan and SAFT images can be compoared. The cross-range resolution can be compared in the right panel of Figure 3.8 the respective profiles are presented.

Transducer	Panametrics 5 MHz
Transducer diameter	10 mm
Water velocity	1480 m/s
Material velocity	4660 m/s
Sampling frequency	80 MHz
Spatial sampling freq.	0.5 mm
Water paths	63.6 mm
Synthetic aperture length	24 mm
B-scan -3dB width	5.2 mm
SAFT -3dB width	3.4 mm
d/2	5 mm

Table 3.4: Test parameters of the immersion test of copper block I

Copper Block II

The copper block II with more coarse structure than that of copper block I was inspected in immersion. This block also has a number of SHDs with diam. 1 mm drilled at different depths from the upper surface. The SDHs located at the depths 20 mm, 24 mm, 28 mm and 32 mm were imaged in the test. Due to the material structure a transducer with lower center frequency was chosen for this test. The test parameters are listed in Table 3.5 and the results of this test are shown in Figure 3.9.

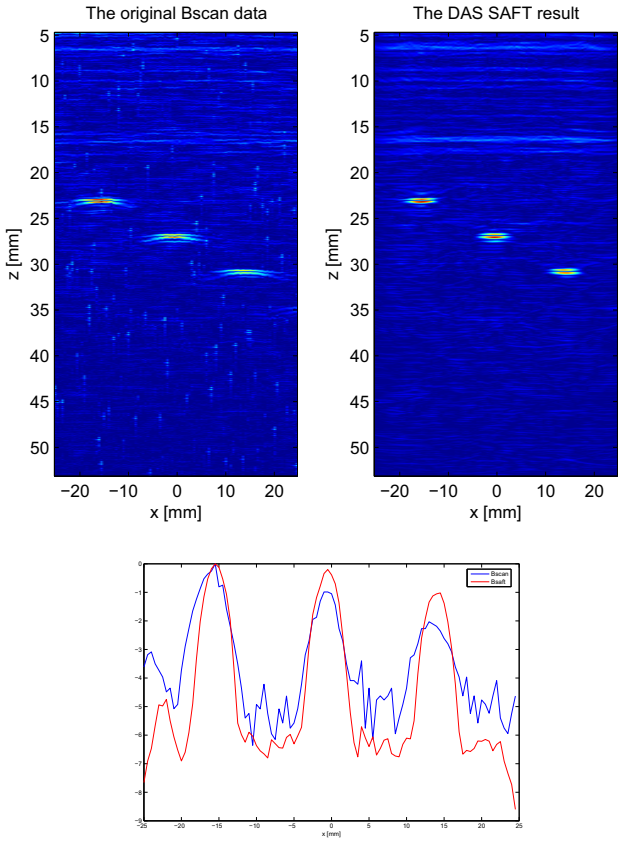

Figure 3.8: Results of the immersion mode test of the copper block I (left) and the cross-range profiles for 3 holes (right). The B-scan and SAFT -3dB widths were respectively, 5.2 mm and 3.4 mm.

Transducer	Panametrics 2.25 MHz
Transducer diameter	10 mm
Water velocity	1480 m/s
Material velocity	4660 m/s
Sampling freq.	80 MHz
Spatial sampling frequency	0.5 mm
Water paths	63.6 mm
Synthetic aperture length	36 mm
B-scan -3dB width	38.4mm
SAFT -3dB width	3.3 mm
d/2	5 mm

Table 3.5: The system parameters of immersion mode test of the copper block II

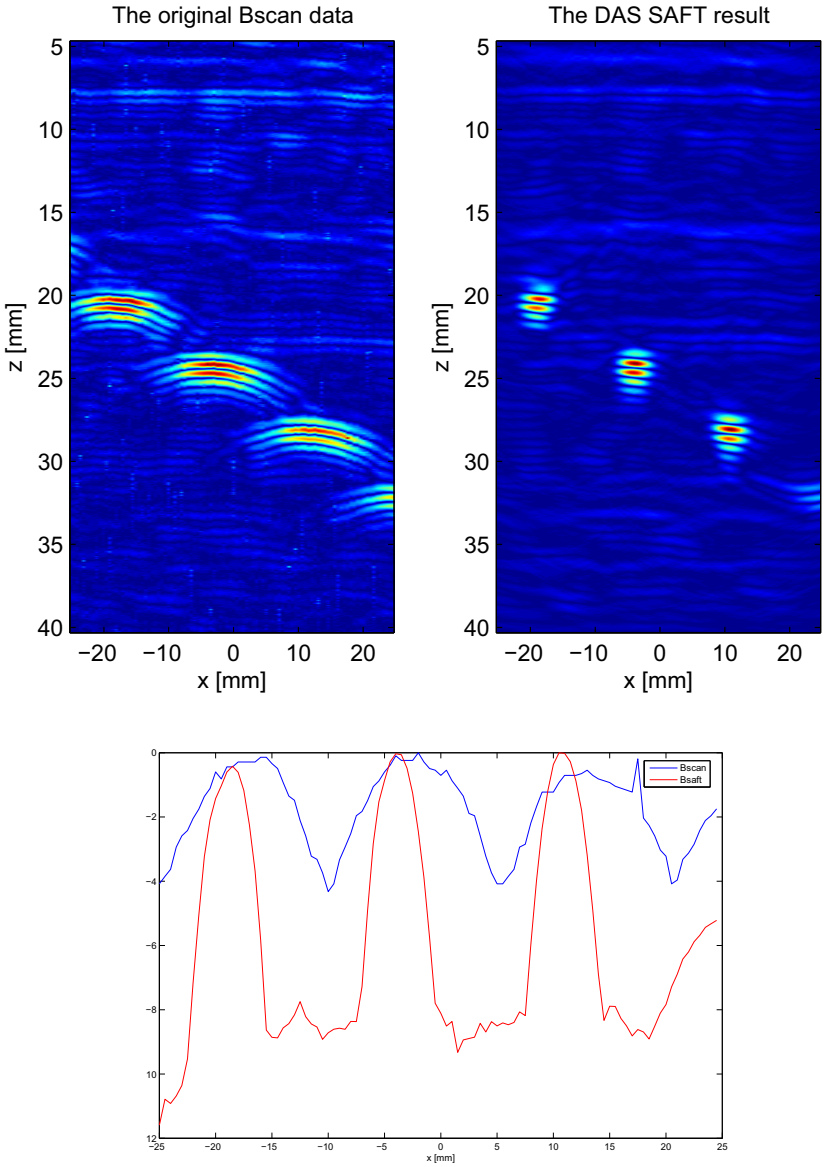

Figure 3.9: Results of the immersion mode test of the copper block I (left) and the cross-range profiles for 3 holes (right). The B-scan and SAFT -3dB widths were respectively, 38 mm and 3.3 mm.

In summary, the t-d SAFT algorithms are capable of improving both the cross-range resolution and suppressing the structure noise. The noise suppression is well pronounced but not such impressive as the resolution improvement. It is expected that the frequency domain SAFT, presented recently [9] could be more effective in this respect.

Chapter 4

Discussion and future work

SAFT algorithms for post-processing ultrasonic data acquired in ultrasonic inspection of coarse structured metals were investigated in this report. SAFT algorithms for contact and immersion inspection were considered and their performance was investigated using real ultrasonic RF signals.

The experimental results presented in this report indicate that the time-domain SAFT algorithms yield considerably improved cross-range (lateral) resolution comparing with the original B-scans for a wide range of target depths. The improved resolution is always better than the theoretical limit for SAFT, equal to half transducer diameter.

As expected, SAFT processing also yields an improved ratio of the ultrasonic defect response to the structure noise level. The observed improvement was in the range of 3 to 5 dB depending on the setup and the test frequency. It is expected that this improvement could be even better if the more efficient frequency-domain SAFT was applied.

It should be pointed out that the classical SAFT schemes considered in this report can be seen as the 2D spatio-temporal filters while the acoustic lens performs the 3D processing of the ultrasonic data. Although extension of the 2D SAFT with third dimension does not present any theoretical problem it is still difficult due to the practical limitations of the today NDE systems as well as the storage and computing resources required for this purpose. The viable solution,already tested by some system manufacturers, seems to be providing the phased array systems with powerful processing resources in real-time to avoid post-processing large data volumes.

The experimental results presented in this preliminary study are positive, that is, SAFT is capable of improving the lateral resolution and suppress structure noise in ultrasonic inspection of coarse structured materials.

The following issues are worth further investigation:

- Acquiring more experimental data,
- Verifying the performance of the frequency-domain SAFT developed recently in our group [9]
- Verifying SAFT using an ultrasonic array instead of a single transducer.

Bibliography

[1] Kefei Lu. Synthetic aperture focusing technique in immerssion mode ultrasonic imaging. Master's thesis, Chalmers University of Technology, 2007.

[2] Jing Liu. Synthetic aperture focusing technique in ultrasonic imaging. Master's thesis, Chalmers University of Technology, 2007.

[3] J.A. Seydel. *Ultrasonic Synthetic-aperture Focusing Techniques in NDT*. Research Techniques for Nondestructive Testing. Academic Press, 1982.

[4] V. Schmitz, S. Chalkov, and W. Muller. Experience with synthetic aperture focusing technique in the field. Ultrasonics, 38:731–38, 2000.

[5] F. Lingvall. *Time domain reconstruction methods for ultrasonic array imaging*. PhD thesis, Uppsala University, Signals and Systems, 2004.

[6] S.R. Doctor, T.E. Hall, and L.D. Reid. Saft – the evolution of a signal processing technology for ultrasonic testing. *NDT International*, 38:165–67, June 1986.

[7] M. Soumekh. *Fourier Array Imaging*. Prentice Hall, 1st edition, 1994.

[8] L.J. Cutrona. Comparison of sonar system performance achievable using synthetic-aperture technique with the performance achievable by more conventional means. *J. Acoust. Soc. Am.*, 58(2):336–348, August 1975.

[9] T. Stepinski. An implementation of synthetic aperture focusing technique in frequency domain. *accepted for IEEE Trans. on Ultrasonics, Ferroelectrics, and Frequency Control*, 2007.

[10] M. Soumekh. *Synthetic aperture radar signal processing*. ohn Wiley & Sons Ltd., 1999.

www.ski.se

STATENS KÄRNKRAFTINSPEKTION
Swedish Nuclear Power Inspectorate

POST/POSTAL ADDRESS SE-106 58 Stockholm
BESÖK/OFFICE Klarabergsviadukten 90
TELEFON/TELEPHONE +46 (0)8 698 84 00
TELEFAX +46 (0)8 661 90 86
E-POST/E-MAIL ski@ski.se
WEBBPLATS/WEB SITE www.ski.se